Journal of Structural Biology 218 (2026) 108377

Contents lists available at ScienceDirect

Journal of Structural Biology

journal homepage: www.elsevier.com/locate/yjsbi

Research Article

Catalytic hydrogen bonds in alcalase–CI-2A complexes revealed by ultra-high-resolution crystallography

Joanna E. Raczynska [a], Robert Jedrzejczak [b,1], Miroslawa Dauter [c], Peter R. Østergaard [d], Keith S. Wilson [e], Wojciech Rypniewski [a,*]

[a] Institute of Bioorganic Chemistry, Polish Academy of Sciences, Noskowskiego 12/14, 61-704 Poznan, Poland
[b] Gdansk University of Technology, Department of Microbiology, Narutowicza 11/12, 80-952 Gdansk, Poland
[c] European Molecular Biology Laboratory (EMBL) Hamburg, c/o DESY, Notkestrasse 85, 22607 Hamburg, Germany
[d] Novozymes AS, Brudelysvej 26, DK-2880 Bagsvaerd, Denmark
[e] Department of Chemistry, University of York, York YO10 5DD, United Kingdom

ARTICLE INFO

Dataset link: PDB ID: 31VH, 31VI and 31VJ. (Original data)

Keywords:
Alcalase
Chymotrypsin inhibitor 2A (CI-2A)
Atomic-resolution crystallography
Hydrogen-bond network
Proton transfer

ABSTRACT

Serine proteases catalyze peptide-bond hydrolysis through a conserved catalytic triad and an extensive network of hydrogen bonds that facilitate proton transfer and stabilization of reaction intermediates. Despite decades of study, the nature of the hydrogen-bonding interactions within the catalytic machinery remains incompletely understood. Here, we report ultra-high-resolution crystal structures of alcalase, a subtilisin-family serine protease, in complex with native chymotrypsin inhibitor 2A (CI-2 A) and with a low-affinity M59P inhibitor variant. The cryogenic structures were determined at 0.74 Å resolution, while an additional 4 °C (277 K) structure of the native complex was determined at 1.05 Å resolution.

The data allowed visualization and refinement of numerous hydrogen atoms within the active site and at the enzyme–inhibitor interface. Comparison of the 4 °C and cryogenic structures revealed a systematic shortening of hydrogen-bond donor–acceptor distances upon cooling, consistent with the global lattice contraction. A notable exception was the hydrogen bond between the catalytic residues Ser221 and His64, which remained unusually short at both temperatures. In the 4 °C structure, the corresponding hydrogen atom is associated with weak and diffuse electron density, suggesting increased proton mobility within this interaction.

The structures further reveal temperature-dependent differences in interactions involving the scissile peptide bond of the inhibitor and the conserved backbone carbonyl oxygen of Ser125. These observations support a model in which Ser125 participates in a concerted hydrogen-bond network coupled to proton transfer within the catalytic triad. Together, the results provide atomic-level insights into hydrogen bonding, protonation equilibria, and catalytic mechanism in subtilisin-like serine proteases.

1. Introduction

Serine proteases constitute one of the largest and most extensively studied classes of proteolytic enzymes (Di Cera, 2009). They catalyze peptide-bond hydrolysis through a conserved catalytic mechanism involving a Ser-His-Asp catalytic triad, in which the serine residue acts as the nucleophile, histidine functions as a general acid–base catalyst, and aspartate modulates the protonation state of histidine. The reaction proceeds through tetrahedral and acyl–enzyme intermediates whose stabilization is facilitated by the oxyanion hole, a structural feature that donates hydrogen bonds to the negatively charged reaction intermediates (Hedstrom, 2002).

Despite decades of biochemical, structural, and computational investigations, several aspects of serine protease catalysis remain debated. In particular, the roles of short hydrogen bonds, proton-transfer equilibria within the catalytic triad, and the coupling between hydrogen-bond networks and catalytic function continue to be actively investigated. High-resolution crystallography provides a powerful approach for addressing these questions by enabling detailed characterization of active-site geometry and, in favorable cases, visualization of hydrogen

* Corresponding author at: Institute of Bioorganic Chemistry, Polish Academy of Sciences, Noskowskiego 12/14, 61-704 Poznan, Poland.
E-mail address: wojtekr@ibch.poznan.pl (W. Rypniewski).
[1] Present address: Eli Lilly and Company, Lilly Corporate Center, Indianapolis, IN 46285, USA.

https://doi.org/10.1016/j.jsb.2026.108377
Received 26 June 2026; Received in revised form 7 September 2026; Accepted 24 September 2026
Available online 25 September 2026
1047-8477/© 2026 The Authors. Published by Elsevier Inc. This is an open access article under the CC BY license (http://creativecommons.org/licenses/by/4.0/).

atoms involved in catalysis.

The nature of the catalytic His-Asp interaction remains a subject of debate. Frey (Frey et al., 1994; Frey, 2004) proposed that upon protonation of histidine, a low-barrier hydrogen bond (LBHB) is formed. LBHBs are characterized by a short donor–acceptor distance and a proton positioned approximately midway between the donor and acceptor atoms, resulting in a highly stabilized hydrogen bond with substantial proton sharing (Cleland et al., 1998). A significant shift of the histidine–bound hydrogen atom toward the aspartate acceptor was observed in the 0.78 Å resolution structure of subtilisin (Kuhn et al., 1998). An alternative interpretation is that the interaction corresponds to a strong hydrogen bond (Fuhrmann et al., 2006; Ishida, 2006). According to Schutz and Warshel (Schutz and Warshel, 2004), LBHBs cannot be unambiguously identified by X-ray diffraction, because their defining structural features are also characteristic of strong ionic hydrogen bonds. LBHB have been reviewed recently by Kemp et al. (Kemp et al., 2021).

An extensive comparison of the active sites of serine hydrolases (Derewenda et al., 1994) revealed the presence of a hydrogen bond between the Cε1 atom of the catalytic histidine and a backbone carbonyl oxygen atom. This interaction is conserved not only in the chymotrypsin and subtilisin families of serine proteases, but also in acetylcholinesterases and other lipases. The authors proposed that this hydrogen bond facilitates acid-base catalysis. Despite its remarkable conservation, the structural and mechanistic significance of this interaction remains poorly understood.

Subsequently, a reaction-driven histidine ring-flip mechanism was proposed by Ash et al. (Ash et al., 2000) to account for this interaction; however, this hypothesis has not gained widespread acceptance (Ishida and Kato, 2003; Topf et al., 2002; Topf and Richards, 2004). Later, quantum mechanical calculations on trypsin further supported the importance of this interaction for efficient catalysis (Fuhrmann et al., 2006), although its precise mechanistic role remains unclear.

Because hydrogen atoms scatter X-rays only weakly, information about their positions can only be obtained from crystallographic data collected at sufficiently high resolution. Ultra-high-resolution structures therefore provide a unique opportunity to investigate hydrogen-bonding interactions and protonation states in enzyme active sites.

Alcalase is a subtilisin-type serine endopeptidase (EC 3.4.21.14) derived from *Bacillus licheniformis* (Smith et al., 1968), featuring a classic catalytic triad (Asp32, His64, and Ser221) that cleaves peptide bonds at the C-terminal side of hydrophobic and aromatic residues. CI-2A is a small, naturally occurring plant protein found in barley (*Hordeum vulgare*) (McPhalen and James, 1987). It belongs to the potato inhibitor I family and inhibits subtilisin-like and chymotrypsin-like proteases. Although the reactive-site loop of CI-2A binds to the protease active site in a canonical, substrate-like manner, the inhibitor resists proteolytic degradation through structural and dynamic features that hinder productive progression of the bound complex toward peptide-bond cleavage (Wei et al., 2019).

Here, we report ultra-high-resolution (0.74 Å) structures of alcalase in complex with native chymotrypsin inhibitor 2A (CI-2A) at 100 K (nat100K), together with a corresponding structure of the M59P inhibitor variant (mut100K), whose affinity for alcalase is approximately five orders of magnitude lower than the wild-type inhibitor. In addition, we present an atomic-resolution (1.05 Å) 4 °C structure of the native complex (nat277K).

These structures enable a detailed comparison of active-site geometry, hydrogen-bonding interactions, and hydrogen-atom positions as a function of temperature and inhibitor binding mode, providing new insights into proton transfer, short hydrogen bonds, and the catalytic hydrogen-bond networks in serine protease catalysis.

2. Results

2.1. Overall structure

Alcalase adopts the characteristic α/β fold of the subtilase superfamily, comprising a twisted central seven-stranded parallel β-sheet surrounded by α-helices and connecting loops. The catalytic triad (Asp32, His64, and Ser221) is situated in a surface-accessible cleft formed by residues contributed by different regions of the polypeptide chain (Fig. 1). CI-2A also adopts a compact α/β fold, consisting of a four-stranded mixed β-sheet (strands 1, 2, 4, and 5) packed against a single α-helix. On the opposite face of the β-sheet lies the exposed reactive-site loop, which contains the P1–P1′ scissile peptide bond and includes β-strand 3, and mediates binding to the protease active site.

The high resolution of the X-ray data enabled unrestrained refinement of many active-site bond lengths and angles, thereby yielding unbiased and highly accurate structural parameters. A summary of the data collection and refinement statistics is provided in Table 1.

Most hydrogen atoms relevant to catalysis were identified in the sharpened $2mF_o–DF_c$ electron density map (see Methods) and subsequently refined freely with isotropic temperature factors, converging to stable positions consistent with chemically reasonable donor–hydrogen–acceptor geometries. A blocked-matrix least-squares refinement (performed in SHELXL) provided estimated standard uncertainties for interatomic distances, as well as for bond and torsion angles, including those involving hydrogen atoms.

A detailed comparison of the three structures revealed differences in hydrogen-bonding geometry, hydrogen-atom positions, and side-chain conformations within the active site.

2.2. Temperature-related effects

Cryocooling was accompanied by a reduction in unit-cell volume from 73,394 $Å^3$ in nat277K to 70,838 $Å^3$ and 70,856 $Å^3$ in nat100K and mut100K, respectively, corresponding to a decrease of approximately 3.5%. A comparison of hydrogen-bond donor–acceptor distances reveals a similar temperature-dependent effect. Consistent with this contraction, the mean hydrogen-bond donor–acceptor distance decreased from 2.94 Å in nat277K to 2.89 Å in the two 100 K structures, corresponding to an average shortening of approximately 0.05 Å (1.7%). Thus, hydrogen bonds are systematically shorter in the cryogenic structures.

2.3. Catalytic-site residues and hydrogen-bond geometry

A particularly short hydrogen bond was observed between the Oγ atom of Ser221 and Nε2 of His64 (Table 2). In both 100 K structures, a weak (approximately 2.7σ) difference electron density peak was observed in the vicinity of the Oγ atom of Ser221 (Fig. 2a). Consequently, the Hγ atom was incorporated into the model and refined, yielding O—H lengths in the range 0.80–0.88 Å. These values are somewhat shorter than the standard dictionary value of 0.95 Å for a hydroxyl group.

In the 4 °C (277 K) structure, a small and diffuse electron density peak was observed, displaced from the canonical position at Oγ toward His64 (Fig. 2b). When Hγ was modeled at the canonical position on Ser221 and refined without restraints, it shifted to a position characterized by an implausible C–O–H angle of 91(4)° and an O—H distance of 1.10(8) Å. In contrast, when the initial position was defined at the Nε2 atom of His64, the hydrogen atom refined to a more chemically reasonable position, with a Nε2–Hε2 bond length of 1.03(12) Å.

To evaluate whether the 4 °C structure provides evidence for protonation of His64, the geometry of the imidazole ring was examined. However, no definite conclusions could be drawn, possibly due to the limited resolution of the 4 °C data. Although individual atoms are clearly resolved as distinct electron-density peaks in all three structures, relatively high electron density was also observed between atoms Cε1 and

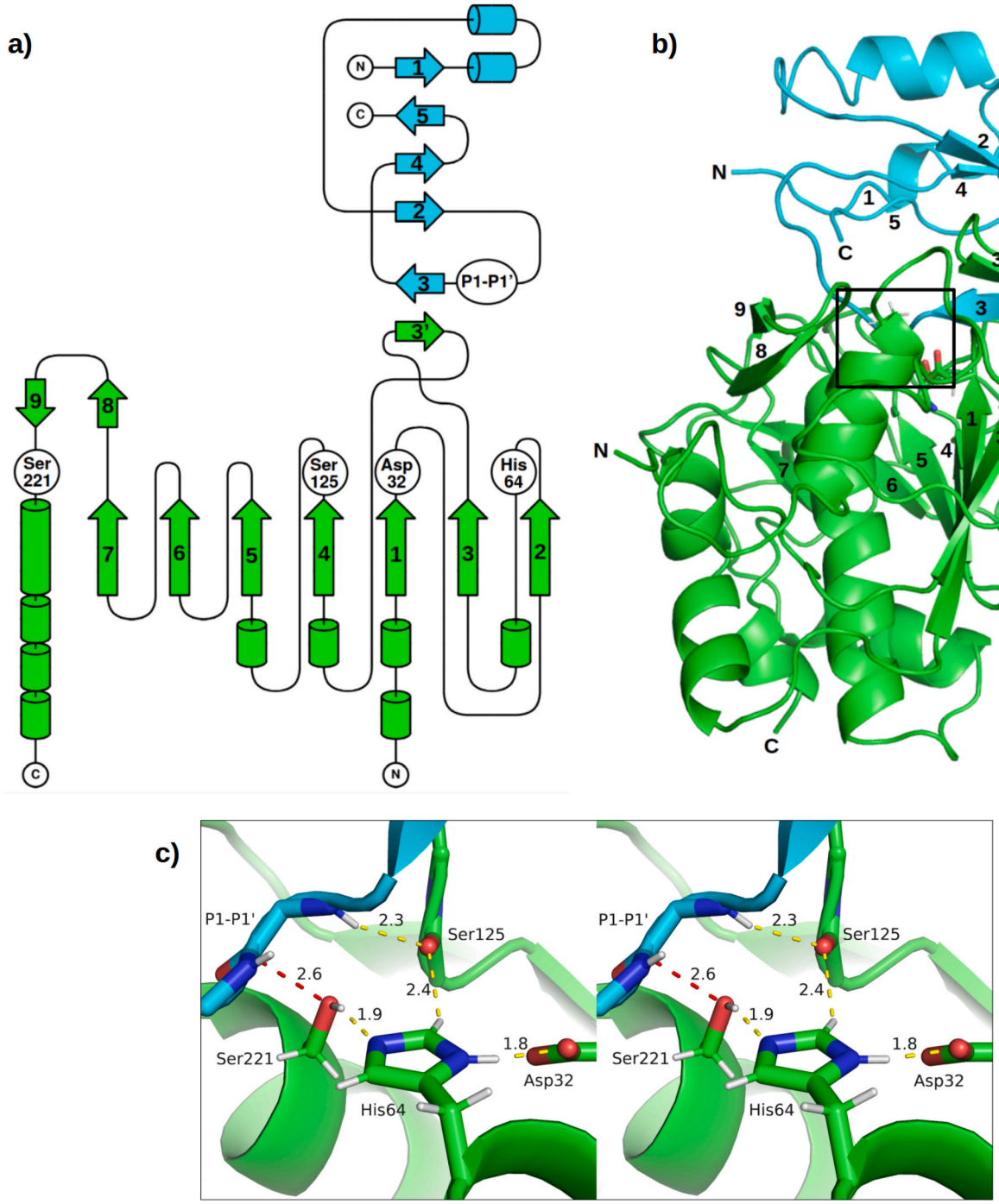


Fig. 1. **(a)** Topology diagrams of alcalase (*green*) and CI-2A (*cyan*). **(b)** Cartoon representation of the alcalase–CI-2A complex. The black rectangle indicates the region shown in detail in **(c)**. **(c)** Stereoview of the active site of the nat100K structure, highlighting the key catalytic residues and their interactions with the P1–P1' scissile peptide bond of CI-2A. Hydrogen bonds are depicted as *yellow* dashed lines, and the putative nucleophilic attack trajectory between the Oγ atom of Ser221 and the carbonyl carbon atom of the scissile bond is shown in *red*. Distances are given in ångströms (Å). (For interpretation of the references to colour in this figure legend, the reader is referred to the web version of this article.)

Nε2, consistent with a Cε1═Nε2 double bond in the catalytic His64 residue. In contrast, electron density between other atoms of the imidazole ring was observed at levels 20–30% lower (Fig. S1).

The refined geometry of the His64 imidazole ring was examined and compared among the nat277K, nat100K and mut100K structures (Table S1). In all three structures, the Cε1–Nε2 bond is the shortest C—N bond in the ring, with lengths of 1.28(7), 1.31(7), and 1.31(7) Å for nat277K, nat100K, and mut100K, respectively. These values are consistent with substantial Cε1–Nε2 double-bond character. However, the differences relative to the other C—N bonds are not statistically significant within the estimated uncertainties.

Atomic displacement parameters (B factors) of the Nδ1 and Nε2 atoms of the catalytic His64 residue were examined for evidence of an unusual charge distribution within the imidazole ring. In the nat277K structure, the B factors of Nδ1 and Nε2 are 5.09(16) $Å^2$ and 6.77(20) $Å^2$, respectively, compared with an average value of 5.67(4) $Å^2$ for the imidazole ring. In the nat100K structure, the corresponding values are 3.61(3) $Å^2$ for Nδ1 and 4.39(4) $Å^2$ for Nε2, with an average B factor of

Table 1
Summary of X-ray data and refinement statistics.

Structure	nat277K	nat100K	mut100K
PDB code	31VH	31VI	31VJ
Space group	P1	P1	P1
Unit cell parameters [Å, °]:			
a	38.27	37.74	37.78
b	45.09	44.53	44.52
c	46.73	46.21	46.18
α	104.0	103.9	103.7
β	101.4	101.2	101.3
γ	103.2	103.1	103.2
Wavelength [Å]	0.9280	0.8020	0.8020
Temperature [K]	277	100	100
Resolution [Å]	10.0–1.05 (1.07–1.05)[a]	25.0–0.74 (0.75–0.74)	25.9–0.74 (0.75–0.74)
R_{merge} [b]	0.063 (0.501)	0.041 (0.133)	0.047 (0.154)
No. observations	621,938	2,635,477	2,665,548
No. unique data	126,230	358,350	358,975
<I/σ(I)>	15.5 (1.6)	26.8 (9.1)	27.5.(7.0)
% completeness	95.0 (88.7)	98.2 (95.1)	98.4 (95.6)
Refinement program	SHELXL		
R1 [c]	0.1101	0.0892	0.0952
wR2 [d]	0.2412	0.2440	0.2584
r.m.s. d. from ideal			
bond lengths [Å]	0.015	0.011	0.012
angles [°]	1.95	1.92	1.85
Average B-value, all atoms [Å^2]	15.0	8.0	9.0

[a] Numbers in brackets refer to the highest resolution shell.
[b] $R_{merge} = \sum_{hkl} \sum_i |I_i(hkl) - < I(hkl) > | / \sum_{hkl} \sum_i I_i(hkl)$, where $I_i(hkl)$ and $< I(hkl) >$ are the observed individual and mean intensities of a reflection with the indices *hkl*, respectively, $\sum_i$ is the sum over *i* measurements of a reflection with the indices *hkl*, and $\sum_{hkl}$ is the sum over all reflections.
[c] $R1 = \Sigma_{hkl} ||F_{obs}| - |F_{calc}|| / \Sigma_{hkl} |F_{obs}|$, where F_{obs} and F_{calc} are the observed and calculated structure factors, respectively.
[d] $wR2 = \{\Sigma_{hkl} [w(F_o^2 - F_c^2)^2] / \Sigma [w(F_o^2)^2]\}^{1/2}$, where *w* is the weighting scheme based on the standard uncertainty $\sigma(F_o^2)$.

3.94(0) Å^2 for the ring. Although the temperature factors of the nitrogen atoms differ significantly both from the ring average and from those of the neighboring atoms (data not shown), these deviations cannot be unambiguously attributed to differences in electron density arising from an unusual charge distribution. Rather, they may reflect variations in the vibrational motion of individual atoms within the imidazole ring.

In addition to the strong hydrogen bond between Oγ_Ser221 and Nε2_His64, another equally strong (short) hydrogen bond is the catalytically important interaction involving Nδ1_His64 and Oδ1_Asp32. The donor–acceptor distance is approximately 2.7 Å in all structures. The Hδ1 atom was identified in the electron density map, and its refined position differs between the low- and 4 °C structures. In nat277K, the N—H length is 0.95(9) Å, whereas in the two 100 K structures it is 0.81–0.82(5) Å (Table 2). However, the difference only corresponds to ~1.3 estimated standard uncertainties (e.s.u., $(0.09^2 + 0.05^2)^{1/2}$) and is therefore unlikely to be significant.

Another notable interaction is the Cε1–Hε1···O hydrogen bond between His64 and the backbone carbonyl oxygen atom of Ser125. The distance between the carbon and oxygen atoms is similar in all three structures and does not exceed 3.18 Å, consistent with a weak C–H···O hydrogen bond (Table 2). The refined Cε1–Hε1 bond lengths are longer in the low-temperature structures; however, the corresponding difference amounts only to approximately 1.5 e.s.u. and is therefore likewise unlikely to be significant.

The oxyanion hole in alcalase is formed by the backbone amide group of Ser221 and the side chain amide of Asn155. In all structures, the carbonyl oxygen atom of the P1 residue (Met59i in the native inhibitor and Pro59i in the mutant) remains engaged in short hydrogen bonds with both donors, with donor–acceptor distances below 3 Å.

All H-bond parameters are summarized in Table 2.

2.4. Geometry of the reactive site

The distance (d_{attack}) between the nucleophilic Oγ atom of Ser221 and the carbonyl carbon atom (C_59i) of the scissile peptide bond is shorter than the sum of the corresponding van der Waals radii (3.2 Å) in all three structures (Table 3). In the native complexes, this distance is substantially shorter than in the mutant complex.

The nucleophilic attack parameters, d_{attack}, α_{attack} and φ_{attack} (Fig. 3), for the two wild-type structures (nat277K and nat100K), are close to the

Table 2
Hydrogen bond parameters [Å,°].

interaction	nat277K				nat100K				mut100K			
	d(D···A)	*d(D—H)*	*d(H···A)*	*D-H···A*	*d(D···A)*	*d(D—H)*	*d(H···A)*	*D-H···A*	*d(D···A)*	*d(D—H)*	*d(H···A)*	*D-H···A*
catalytic residues												
Oγ_Ser221	2.664(10)	1.03(12)	1.67(13)	158(9)	2.659(3)	0.80(5)	1.88(5)	164(5)	2.740(3)	0.88(6)	1.86(6)	171(6)
Nε2_His64												
Nδ1_His64	2.730(9)	0.95(9)	1.79(9)	168(8)	2.677(3)	0.82(5)	1.87(5)	170(4)	2.712(3)	0.81(5)	1.91(5)	168(5)
Oδ1_Asp32												
Cε1_His64	3.183(11)	0.81(10)	2.54(10)	138(9)	3.138(4)	0.91(5)	2.41(5)	137(4)	3.147(4)	0.98(5)	2.26(5)	150(4)
O_Ser125												
P1 amide												
N_Met59i	2.931(9)	0.81(10)	2.39(10)	125(8)	2.885(4)	0.83(5)	2.49(5)	110(4)	–	–	–	–
Oγ_Ser221												
N_Met59i	3.375(9)	0.81(10)	2.64(10)	152(9)	3.145(3)	0.83(5)	2.34(5)	163(5)	–	–	–	–
O_Ser125												
oxyanion hole												
N_Ser221	2.974(8)	0.93(8)	2.06(9)	171(7)	2.948(4)	0.85(5)	2.13(4)	160(4)	2.910(3)	0.98(4)	1.96(4)	163(4)
O_Met/Pro59i												
Nδ2_Asn155	2.870(11)	0.93(12)	2.03(13)	148(10)	2.847(4)	0.83(6)	2.10(6)	150(5)	2.896(4)	0.98(6)	2.06(6)	142(5)
O_Met/Pro59i												
P1' amide												
N_Glu60i	2.688(14)	1.10(11)	1.85(11)	130(7)	2.619(8)	0.88(6)	2.02(6)	124(5)	–	–	–	–
Oε1_Glu60i												

d(D···A) – donor–acceptor distance; d(D—H) – donor–hydrogen distance; d(H···A) – hydrogen–acceptor distance; D-H···A – hydrogen bond angle.

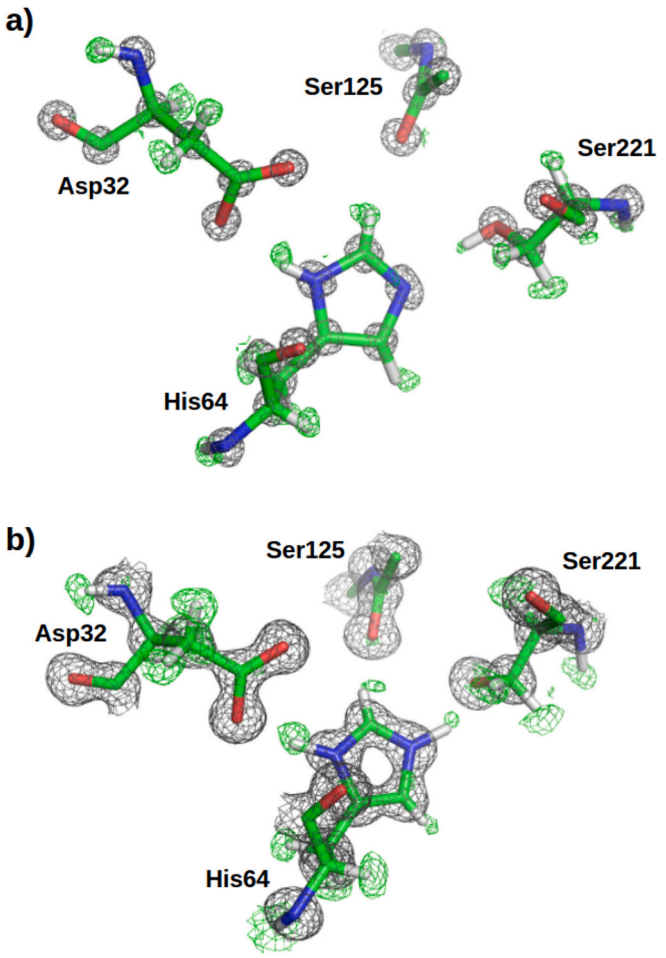


Fig. 2. The catalytic residues in (**a**) nat100K and (**b**) nat277K, shown with the corresponding electron-density. The 2mFo-DFc map is depicted in black and contoured at 2σ, whereas the sharpened (see Methods) mFo-DFc map is shown in green and contoured at 2.7 σ in panel (**a**) and 2.5 σ in panel (**b**). The maps were calculated with hydrogen atoms in the active site omitted. Peaks in the green map approximately coincide with the final refined positions of the hydrogen atoms, shown as white sticks. (For interpretation of the references to colour in this figure legend, the reader is referred to the web version of this article.)

values of 2.68 Å, 93° and 84°, respectively, derived from a large ensemble of serine-protease structures (Du et al., 2025). In contrast, the corresponding parameters for the mut100K structure deviate significantly from these consensus values. Furthermore, the Nε2_His64–Oγ_Ser221–C_Met59i angles are 107.0°, 107.9°, and 110.5° in nat277K, nat100K, and mut100K, respectively, all close to the ideal tetrahedral angle of 109.5° expected for an sp^3-hybridized oxygen atom. The carbonyl carbon atom (C_59i) exhibits measurable pyramidalization in all three structures. The displacement is directed toward the nucleophile, as expected for incipient tetrahedral character, and reaches significant values in each case (Table 3). The Ser221 side chain rotates by approximately 4° about the χ1 torsion angle between the native and mutant complexes. This movement partially compensates for the altered position of the inhibitor in mut100K by shifting the Oγ atom toward the displaced carbonyl carbon atom.

To assess the extent of perturbation of the scissile peptide bond, its internal geometry was examined. No significant differences were observed in the carbonyl C═O bond lengths. In contrast, the peptide C—N bond is longest in nat277K (1.354(13) Å), whereas the corresponding distances in nat100K and mut100K are 1.320(4) Å and 1.332 (4) Å, respectively, closer to the ideal value of 1.329 Å. Analysis of the

Table 3
The nucleophilic attack geometry.

	nat277K	nat100K	mut100K
d_{attack} [Å] *	2.682(9)	2.605(3)	2.916(4)
α_{attack} [°] †	93.5(5)	93.75 (15)	82.79 (18)
φ_{attack} [°] ‡	81.80 (41)	82.59 (13)	88.65 (13)
Pyramidalization [Å] ¶	0.042(9)	0.053(3)	0.041(3)
χ^1_{Ser221} [°] £	81.50 (75)	82.09 (22)	77.55 (24)
Deviation of H_60i atom from the scissile peptide plane [Å] §	−0.23 (10)	0.06(6)	0.15(6)

* Distance between the nucleophilic and the electrophilic atoms (Oγ_Ser221–C_59i).
† Angle formed by the nucleophilic atom, the electrophilic atom and the carbonyl oxygen atom (Oγ_Ser221–C_59i–O_59i).
‡ Dihedral angle between two planes: (i) the plane defined by the nucleophilic atom (Oγ_Ser221), the electrophilic atom (C_59i) and the carbonyl oxygen atom (O_59i), and (ii) the plane of the reactive amide carbonyl. See Fig. 3 for a graphical definition of d_{attack}, α_{attack} and φ_{attack}.
¶ Distance between C_59i and the peptide plane defined by N_60i, Cα_59i and O_59i.
£ χ^1_{Ser221} is the torsion angle (N–Cα–Cβ–Oγ) of the catalytic Ser221.
§ The scissile peptide plane is defined by C_59i, O_59i, N_60i, Cα_60i [Å].

peptide-bond angles revealed that only the C_59–N_60–Cα_60 angle in nat277K, at 118.2(9)°, deviates significantly from the typical value of 121.7°.

An electron density peak corresponding to H_Glu60i was observed, and the refined N—H bond lengths are 1.10(11), 0.88(6) and 0.90(6) Å for nat277K, nat100K, and mut100K, respectively.

In nat277K, the hydrogen atom is displaced by 0.23(10) Å from the peptide-bond plane toward His64. In contrast, in the two 100 K structures it lies close to the plane and is displaced in the opposite direction, by 0.06(6) Å in nat100K and 0.15(6) Å in mut100K.

The amide group of the P1 residue (Met59i) participates in hydrogen-bonding interactions with both the Oγ atom of catalytic Ser221 and the backbone carbonyl oxygen atom of Ser125 (Fig. 4). The donor–acceptor distance between N_Met59i and Oγ_Ser221 is 2.931(9) Å in nat277K and to 2.885(4) Å in nat100K. The N—H bond length of the P1 amide refined to comparable values in the two structures, namely 0.81(10) Å for nat277K and 0.83(5) Å for nat100K.

In contrast, the N_Met59i···O_Ser125 distance increases from 3.145 (3) Å in nat100K to 3.375(9) Å in nat277K. The latter value lies at the upper limit generally considered compatible with hydrogen-bond formation. The difference exceeds 20 estimated standard uncertainties (e.s.u.) and is therefore unequivocally significant. In contrast, analysis of the adjacent Thr58i–Met59i peptide group revealed no significant deviations in bond lengths or bond angles (Table S2), indicating that the structural changes are localized to the hydrogen-bonding environment of the P1 amide.

2.5. Conformational differences in CI-2A

Glu60i occupies the P1′ position immediately adjacent to the scissile bond (Met59i–Glu60i). In the nat277K structure, its side chain adopts a curled conformation stabilized by hydrogen bonds involving Oε1 of Glu60i and both its own backbone amide group and the hydroxyl group of Thr58i (Fig. 4). In the nat100K structure, the side chain is statically disordered and adopts two alternative conformations. The curled conformation is present with an occupancy of 0.3, whereas the predominant conformation is extended. In the mut100K structure, only the extended conformation is observed. Thus, the intramolecularly hydrogen-bonded curled conformation is most prominent in the nat277K structure, less populated in nat100K, and absent in mut100K.

Substitution of Met59i by Pro results in increased backbone rigidity,

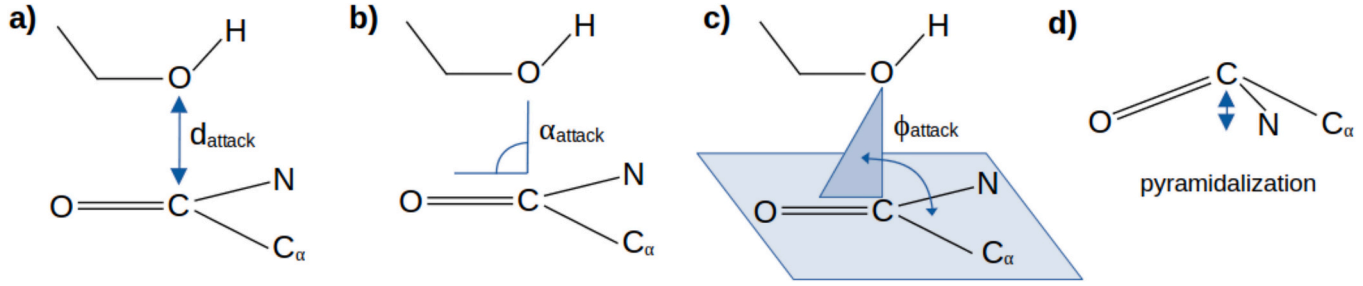


Fig. 3. Definition of the nucleophilic attack parameters. **(a)** d_{attack} is the distance between the nucleophilic and the electrophilic atoms. **(b)** α_{attack} is the angle formed by the nucleophilic atom, the electrophilic atom and the carbonyl oxygen atom. **(c)** φ_{attack} is the angle between two planes: (i) the plane defined by the nucleophilic atom, the electrophilic atom and the carbonyl oxygen atom, and (ii) the plane of the reactive amide carbonyl group. **(d)** Pyramidalization is the perpendicular distance between the electrophilic carbon and the peptide plane defined by N–C_α–O. The diagrams were prepared following the definitions of (Du et al., 2025).

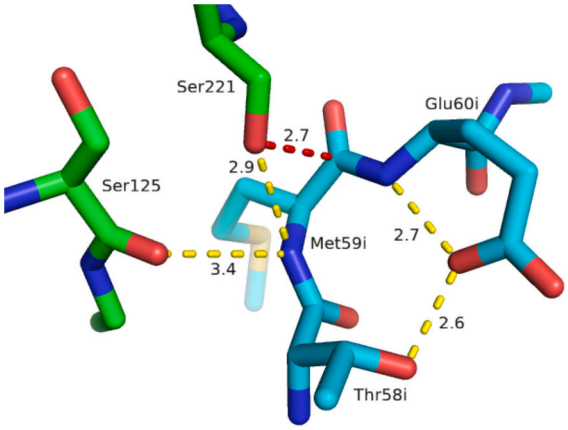


Fig. 4. Environment of the P1–P1′ peptide bond in the nat277K structure. Carbon atoms of the CI-2A inhibitor and catalytic Ser221 are shown in *cyan* and *green*, respectively. The side chain of Glu60i (P1′) forms hydrogen bonds (*yellow* dashed lines) with its backbone amide group and the side chain of Thr58i. The amide group of Met59i (P1) participates in hydrogen bonding with the Oγ atom of Ser221 and forms a weaker hydrogen bond with the backbone carbonyl oxygen atoms of Ser125. The putative nucleophilic interaction between Ser221 Oγ and the carbonyl carbon atom of the scissile peptide bond is shown as a *red* dashed line. Distances are given in ångströms (Å). (For interpretation of the references to colour in this figure legend, the reader is referred to the web version of this article.)

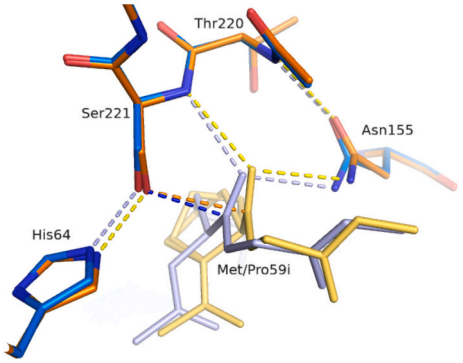


Fig. 5. Superposition of the nat100K (enzyme, *dark blue*; inhibitor, *light blue*) and mut100K (enzyme, *orange*; inhibitor, *yellow*) structures. The altered binding mode induced by the M59P substitution at the P1 position is accompanied by rotation of the Ser221 side chain and a compensatory shift of the His64 imidazole ring. The geometry of the oxyanion hole remains largely preserved through a corresponding displacement of the Asn155 side chain, which maintains interactions with the carbonyl oxygen atom of the P1 residue. Hydrogen bonds are depicted as *light-blue* and *yellow* dashed lines in the nat100K and mut100K structures, respectively. The putative nucleophilic interaction between Ser221 Oγ and the carbonyl carbon atom of the P1 residue is shown in *dark blue* and *orange*, respectively. (For interpretation of the references to colour in this figure legend, the reader is referred to the web version of this article.)

altered local conformation, and loss of the amide hydrogen atom at the P1 position. In the mut100K structure, the reactive-site loop adopts a tighter turn than in the nat277K and nat100K structures. In the mutant structure, this turn is stabilized by a hydrogen bond between O_Thr58i and N_Glu60i, an interaction absent in the native inhibitor. In addition, the proline residue at the P1 position forms fewer van der Waals contacts with the enzyme than the methionine residue in the native complex.

Superposition of Cα atoms with the nat100K structure shows that the largest positional deviations within the inhibitor occur on both sides of the scissile bond (Fig. 5). An exception is the O_Pro59i atom, whose position differs by only 0.30 Å, likely reflecting tight binding within the oxyanion hole. A compensatory shift is observed for Nδ2 of Asn155, a component of the oxyanion hole, such that its interaction with O_Pro59i, which occupies the oxyanion hole, remains nearly unchanged relative to the wild-type structure (Table 2).

In contrast, the position of the carbonyl carbon atom of Pro59i, the target of nucleophilic attack, differs by as much as 0.6 Å between the nat100K and mut100K structures. Although the Ser221 side chain undergoes a compensatory rotation (Fig. 5), the Oγ_Ser221–C_Pro59i distance remains significantly longer in the mutant complex (Table 3). Notably, the adjustment of the nucleophilic oxygen is achieved through side-chain rotation rather than translational displacement of the catalytic serine. This behavior is consistent with the mechanism proposed for trypsin by Du et al., in which rotation of the catalytic serine side chain shortens the reaction coordinate while avoiding larger structural rearrangements (Du et al., 2025).

Finally, a modest reorientation of the His64 imidazole ring is observed. The angle between the ring planes in nat100K and mut100K is approximately 7°, with the largest positional shifts occurring at atoms Cδ2 and Nε2.

3. Discussion

3.1. Temperature-dependent structural changes and interactions among the catalytic residues

Cryocooling greatly facilitates crystallographic data collection by reducing radiation damage and extending crystal lifetime. However, it can also introduce structural artifacts that may bias the biological interpretation of crystallographic models (Stachowski and Fischer, 2026). Among the principal consequences of cryocooling are contraction of the crystal lattice and reduced atomic motion, both of which can affect intermolecular distances and conformational equilibria (Juers and Matthews, 2004, 2001).

These effects are evident in the present structures. The average

hydrogen-bond donor–acceptor distance decreases by approximately 0.05 Å (1.7%) upon cooling from 277 K to 100 K. This magnitude is consistent with the well-documented contraction of protein crystals during cryocooling (Juers and Matthews, 2001). The systematically shorter hydrogen bonds observed in the cryogenic structures are therefore most likely a global consequence of cryocooling rather than evidence that individual interactions have become substantially stronger. Accordingly, mechanistic interpretations should rely primarily on relative differences within a given structure and on structural features that are preserved across both temperature regimes.

A notable exception is the hydrogen bond between the catalytic residues His64 and Ser221. Unlike the other hydrogen bonds analyzed, the donor–acceptor interaction of this hydrogen bond remains equally short in both the 277 K and cryogenic structures. Its apparent insensitivity to the global contraction induced by cryocooling suggests that its geometry is maintained by local structural constraints and is consistent with an interaction of particular functional importance within the catalytic machinery. This unusual temperature (in)dependence distinguishes the Ser221-His64 interaction from the remaining hydrogen bonds in the active site and motivates its detailed consideration in the following section.

At the present resolution, most catalytically relevant hydrogen atoms could be refined without geometric restraints. Their refined X–H distances should nevertheless be interpreted with caution because X-ray scattering and atomic motion result in apparent bond lengths shorter than the corresponding internuclear distances. The freely refined X–H bond lengths obtained in the present study are generally consistent, within their estimated standard uncertainties, with the temperature-dependent target values used by SHELXL for riding hydrogen atoms. The only notable exception is the hydrogen atom shared between Ser221 and His64 in the 277 K structure.

Analysis of the nucleophilic attack parameters indicates that Ser221 is optimally positioned to attack the P1 carbonyl carbon atom. Together with the experimental observation that CI-2A undergoes rapid acylation by subtilisin (Radisky and Koshland, 2002), this suggests that inhibitor binding elicits an initial enzymatic response similar to that observed for a true substrate. In the present structures, this initial step appears to involve partial proton transfer from the Ser221 hydroxyl group to the Nε2 atom of His64.

In both 100 K structures, the Hγ atom is clearly associated with Ser221, as evidenced by the electron density (Fig. 1). In the nat277K structure, however, the electron density between Nε2_His64 and Oγ_Ser221 is less well defined. The hydrogen atom refined more satisfactorily when assigned to His64, although the corresponding electron density is weaker than that observed for other hydrogen atoms, rendering its placement uncertain. This ambiguity may be related to the short donor–acceptor distance between Oγ of Ser221 and Nε2 of His64. Among the analyzed hydrogen bonds, this is the only one that remains equally short in both nat277K and nat100K (Table 2), despite the fact that hydrogen bonds are, on average, shorter in the 100 K structures.

Several mechanisms may account for the apparent disorder of a hydrogen atom even within a short hydrogen bond. The proton may occupy two alternative positions corresponding to a double-well potential, undergo rapid transfer between donor and acceptor, or become increasingly delocalized as the donor–acceptor distance decreases. Alternatively, at 4 °C, proton motion along the hydrogen-bond axis may be sufficiently pronounced to produce diffuse electron density. Thus, the weak and diffuse electron density observed for this hydrogen atom may reflect genuine proton mobility within a short His-Ser hydrogen bond, a phenomenon previously discussed for catalytic hydrogen bonds in serine proteases (Agback and Agback, 2018; Fuhrmann et al., 2006).

The geometry of the imidazole ring provides no independent evidence for proton transfer to Nε2. The refined Cε1–Nε2 distance is shorter than those of the other C—N bonds in the His64 imidazole ring. Although this difference is not statistically significant given the relatively large e.s.u. (Table S1), the short Cε1–Nε2 distance, together with the pronounced electron density between Cε1 and Nε2 (Fig. S1), is consistent with substantial Cε1–Nε2 double-bond character. This observation suggests that, if His64 is partially protonated, the excess positive charge would be localized primarily at Nε2.

Taken together, the Ser221-His64 hydrogen-bond geometry and the refined His64 imidazole-ring geometry are compatible with, but do not demonstrate, partial proton transfer from Ser221 to His64.

It has been proposed that the interaction between the catalytic histidine and aspartate residues in serine proteases forms a low-barrier hydrogen bond (LBHB), characterized by a short donor–acceptor distance and a proton positioned approximately midway between the two atoms (Cleland et al., 1998; Frey et al., 1994; Schiøtt et al., 1998). In the two 100 K structures, the hydrogen atom remains closely associated with the donor atom, whereas in nat277K it appears to be shifted toward Oδ1 of Asp32, although the difference is not statistically significant (Table 2). Such a displacement would be consistent with partial proton transfer from His64 to Asp32 and could be expected if this hydrogen bond were to acquire partial LBHB character.

However, in none of the three structures is the donor–acceptor distance sufficiently short to satisfy the criteria generally associated with an LBHB, which typically requires donor–acceptor distances of approximately 2.5–2.6 Å. The observed donor–acceptor distance of ~2.7 Å is therefore consistent with a strong hydrogen bond and does not support an LBHB interpretation.

3.2. Structural coupling of the P1 amide and catalytic site

If partial proton transfer from Ser221 to His64 occurs in the nat277K structure, a greater negative charge density would be expected on the Oγ atom of Ser221 relative to nat100K. This increase should enhance its ability to accept a hydrogen bond from the P1 amide, consistent with the short N_Met59i···Oγ_Ser221 distance observed in both temperature regimes (Fig. 6).

Within the catalytic mechanism, the hydrogen bond between Ser221 Oγ and the P1 amide nitrogen is likely to contribute to stabilization of the first tetrahedral transition state. Quantum-mechanical calculations by Ishida and Kato (Ishida and Kato, 2003) indicate that formation of this transition state is accompanied by increasing negative charge on the catalytic serine oxygen, consistent with enhanced hydrogen-bond acceptance by Oγ and supporting the proposed functional role of this interaction.

Because the P1 amide simultaneously donates a second hydrogen

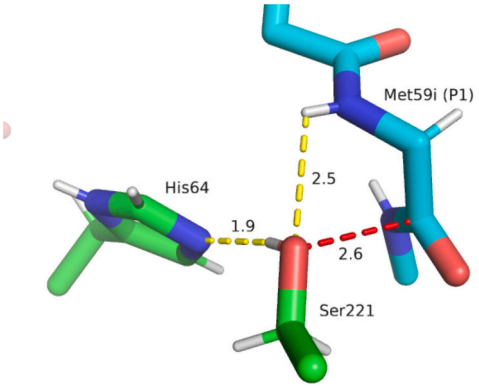


Fig. 6. Interactions of the catalytic Ser221 in the nat100K structure. The Oγ atom of Ser221 approaches the carbonyl carbon atom of the scissile peptide bond (*red* dashed line) while simultaneously forming hydrogen bonds (*yellow* dashed lines) with the catalytic His64 residue and the P1 amide group. Distances are given in ångströms (Å). Some atoms have been omitted for clarity. See Fig. 7 for an illustration of the complete network of interactions. (For interpretation of the references to colour in this figure legend, the reader is referred to the web version of this article.)

bond to the backbone carbonyl oxygen of Ser125, changes in the polarization of this amide group are expected to influence both interactions.

The interactions involving the P1 amide, the catalytic triad residues and Ser125 can be integrated into a model of a concerted hydrogen-bond network (Fig. 7), in which changes in hydrogen-bond strengths are coupled to redistribution of charge within the catalytic machinery. This model is consistent with both (i) the substantially longer hydrogen bond between O_Ser125 and the amide nitrogen (N_Met59i) of the scissile peptide bond in nat277K compared with nat100K (3.38 Å vs 3.15 Å; Table 2) and (ii) the proposed partial proton transfer from Ser221 to His64 in the 4 °C structure.

It has been suggested that the interaction between the Cε1 atom of the catalytic histidine and the backbone carbonyl oxygen atom of Ser125 increases the electronegative character of Nε2, thereby facilitating protonation of the histidine residue (Derewenda et al., 1994). While such an effect may stabilize the protonation state of His64, it would also be expected to oppose proton donation by histidine during general acid catalysis. We therefore suggest that the His64-Ser125 interaction may be dynamically modulated during the catalytic cycle, stabilizing protonated His64 during the general base catalysis and weakening during the subsequent general acid step, thereby facilitating proton transfer to the leaving group. Fig. 7 illustrates a possible role of this interaction during the acylation phase of the hydrolysis reaction. This model provides a possible mechanistic explanation for the remarkable conservation of the His64-Ser125 interaction among serine hydrolases.

3.3. Consequences of perturbing the reactive-site loop

Previous mutational studies of CI-2 have shown that the P1 (Met59i) residue is the principal determinant of binding affinity, whereas residues at the P1′ position and adjacent sites generally make smaller contributions (Radisky et al., 2004, 2005). Nevertheless, residues at the P1′ position can influence the conformation of the reactive-site loop, the kinetics of association and dissociation, and susceptibility to proteolysis.

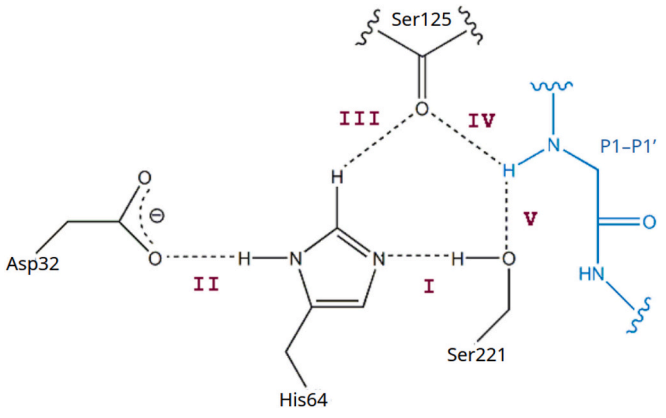


Fig. 7. Concerted network of hydrogen bonds. In the enzyme-substrate (ES) complex, a dynamic equilibrium exists between interactions IV and V. Strengthening of interaction V enhances interaction I through cooperative hydrogen-bonding effects, ultimately promoting proton transfer from Ser221 to His64. In the first transition state (TS1), His64 becomes protonated. The resulting imidazolium ion is stabilized by interactions II and III, both of which are stronger than in the neutral histidine. Strengthening of interaction III weakens interaction IV through competition for hydrogen-bond acceptance. At the same time, interaction V is reinforced by the increased attraction of the Ser221 alkoxide ion, further weakening interaction IV. Upon formation of the acyl–enzyme intermediate, interaction V weakens because resonance stabilization of the ester reduces the basicity of the tetrahedral oxygen atom. Consequently, interaction IV strengthens, whereas interaction III weakens, reducing the stabilization of the imidazolium ion and facilitating its deprotonation. Proton transfer to the amine leaving group further weakens interactions II and III, thereby strengthening interaction IV. In this model, the backbone carbonyl oxygen atom of Ser125 functions as a molecular switch that modulares the protonation state of His64.

Glu60i occupies the P1′ position of the reactive-site loop and contributes to its stabilization through intramolecular hydrogen bonding. In the present structures, the Glu60i side chain adopts alternative conformations and, in one of them, forms a hydrogen bond between its carboxylate group and its own backbone amide nitrogen (Fig. 4). This interaction may contribute to the conformational coupling between the inhibitor reactive site and the catalytic triad and, more generally, to the concerted hydrogen-bond network proposed above (Fig. 7).

In nat277K, the hydrogen-bonded curled conformation of Glu60i is fully occupied, whereas in nat100K it has an occupancy of only ~30%. Correspondingly, the distance between Oγ of Ser221 and the target of its nucleophilic attack, the carbonyl carbon atom of Met59i, is significantly longer in nat277K than in nat100K (Table 3). This correlation raises the possibility that the intra-residue hydrogen bond between N_Glu60i and Oε1_Glu60i (Fig. 4) influences the electronic environment of the scissile peptide bond in a manner that makes nucleophilic approach less favorable.

The M59P substitution restricts the conformational freedom of the reactive-site loop, resulting in a tighter turn around the P1 residue. It also increases the distance between Oγ of Ser221 and the P1 carbonyl carbon, indicating a less favorable geometry for nucleophilic attack. This change is partly compensated by rotation of the Ser221 side chain, reflected in an adjustment of its χ1 torsion that shifts Oγ toward the displaced P1 carbonyl carbon.

Despite the altered binding of the inhibitor, the geometry of the oxyanion hole remains essentially unchanged, as judged by both donor–acceptor and hydrogen–acceptor distances. This preservation is achieved through a compensatory displacement of Asn155 Nδ2, which accommodates the altered position of the inhibitor while maintaining a strong interaction with the oxyanion oxygen atom (Fig. 5). Thus, the M59P substitution perturbs the geometry of nucleophilic attack while leaving the oxyanion-hole interactions largely intact, illustrating the ability of the reactive-site loop and catalytic residues to accommodate local structural changes through compensatory adjustments.

3.4. Conclusions

Taken together, the present ultra-high-resolution structures provide a detailed view of the hydrogen-bonding interactions within the active site of a subtilisin-family serine protease under both cryogenic and 4 °C conditions. The comparison demonstrates that cryocooling produces systematic shortening of hydrogen bonds and highlights the importance of distinguishing global temperature effects from catalytically meaningful structural features.

Beyond these temperature-dependent effects, the structures reveal several observations that appear to be functionally significant, including the unusual behavior of the Ser221-His64 hydrogen bond, the pronounced temperature dependence of the Ser125–P1 amide interaction, and conformational variability of the P1′ Glu60i side chain. Together, these findings are consistent with a model in which hydrogen-bonding interactions within the catalytic machinery are cooperatively coupled, allowing redistribution of electron density to accompany proton transfer and substrate activation during catalysis.

Although the proposed concerted hydrogen-bond network remains a mechanistic hypothesis, it provides a coherent structural framework that accounts for the observed geometrical changes and offers a possible explanation for the remarkable conservation of the His64-Ser125 interaction among serine hydrolases. We anticipate that future neutron diffraction, time-resolved crystallography, and quantum-mechanical studies will further test and refine this model.

4. Materials and methods

4.1. Formation and purification of the Alcalase–CI-2A complex

Alcalase was purified from a commercial Alcalase® preparation obtained from Novozymes (currently Novonesis). Native CI-2A and the M59P inhibitor variant were produced by recombinant expression of the corresponding genes in *Saccharomyces cerevisiae* and purified according to the procedure described in Patent DE69108736T2 (Examples 1 and 3).

Equal amounts of alcalase and CI-2A (either native or M59P mutant) inhibitor were combined in a solution containing 50 mM boric acid, 5 mM succinic acid and 1 mM $CaCl_2$, at pH 6.0 (Buffer A), yielding an approximate inhibitor-to-protease molar ratio of 3:1. The mixture was applied to an S-sepharose HP cation-exchange column pre-equilibrated with Buffer A to separate the alcalase–inhibitor complex from excess unbound inhibitor. The column was extensively washed with Buffer A, and the bound complex was subsequently eluted using a linear NaCl gradient (0 to 500 mM) in Buffer A over five column volumes.

Fractions collected during elution were analyzed by SDS-PAGE, and those exhibiting an approximately 1:1 M ratio of alcalase to inhibitor were pooled to yield the alcalase–CI-2A complexes.

Alcalase displays a broad pH activity profile, with optimal activity at pH 8–9. The experiments described here, including crystallization, were conducted at pH 6, a condition under which the enzyme remains stable for extended periods. Under these conditions, alcalase retains approximately 70% of its maximum activity toward denatured hemoglobin, 55% toward casein, and 16–55% against *p*-nitroaniline (pNA) substrate analogues.

4.2. Crystallization

Crystals were obtained using hanging-drop vapor-diffusion. For the nat277K structure, the initial drop conditions consisted of 12.5 mg/ml protein, 5% *w/v* PEG 4000, 330 mM NaCl, 330 mM citrate buffer at pH 6.0, and 1.5 mM $CaCl_2$. The reservoir solution contained 15% (*w/v*) PEG 4000, 1 M NaCl, 100 mM citrate buffer at pH 6.0, and 5 mM $CaCl_2$. After approximately two months, small crystals emerged among amorphous precipitate and microcrystalline spherulites. Macroseeding was subsequently employed to cultivate larger crystals (approximately 0.3 mm) suitable for atomic-resolution data collection.

For the nat100K and mut100K structures, the protein was prepared in a solution containing 10 mM Hepes at pH 7, 1 mM $CaCl_2$, 100 mM NaCl, at a protein concentration of 10–20 mg/ml. The reservoir solution consisted of 1 M NaCl, 5% *w/v* PEG 6000, 10 mM $CaCl_2$, 100 mM Hepes at pH 6. Crystallization drops were prepared by mixing 3–5 µl of the protein solution with an equal volume of the well solution. Crystals were grown at room temperature.

4.3. Data collection and processing

Diffraction data were collected using synchrotron radiation at the EMBL beamlines at the DORIS storage ring (DESY, Hamburg), employing a MAR Research imaging-plate detector. Data for the nat277K structure were obtained from two crystals, whereas the nat100K and mut100K data were each collected from a single crystal. Data reduction and scaling were carried out using the programs DENZO and SCALEPACK (Otwinowski and Minor, 1997). Structure-factor amplitudes were derived from the measured intensities; however, the original intensity data were retained for refinement with SHELXL (Sheldrick, 2015). A summary of data-collection parameters and the final refinement statistics is provided in Table 1.

4.4. Structure determination

The structure was solved by molecular replacement using the program AMORE (Navaza, 2001) from the CCP4 program suite (Winn et al., 2011). Solutions were obtained independently for the enzyme and the inhibitor. For the enzyme, the structure of subtilisin Carlsberg (PDB ID: 2SEC) was used as the search model, while for the inhibitor, the deposited structure of CI-2 (PDB ID: 2CI2) served as the starting model.

4.5. Refinement

Initial refinement was carried out using REFMAC5 (Murshudov et al., 2011), and solvent molecules were added using ARP/wARP (Langer et al., 2008). Subsequent refinement cycles were performed in SHELXL (Sheldrick, 2015) using a conjugate-gradient least-squares algorithm. Refined parameters included anisotropic atomic displacement parameters and occupancy factors for residues exhibiting multiple conformations, with occupancies constrained to sum to unity. Manual model-building and validation were performed in Coot (Emsley et al., 2010).

Hydrogen atoms were added in riding position, except for those in active-site residues. For hydroxyl and methyl groups, torsion angles was refined to position hydrogen atoms at maxima of electron density, using AFIX 147 and AFIX 137 protocols. After completion of the main refinement stages, active-site hydrogen atoms identified in the mF_o-Df_c sharpened electron density map (calculated in SHELXPRO by scaling map coefficients by $<F^2>^{1/4}$, where $<F^2>$ denotes the mean intensity in a given resolution shell), were incorporated into the model and refined without restraints. At this stage, all restraints on the side chains of active-site residues, as well as on the relevant main-chain atoms of the P1 and P2 residues of CI2A, were also removed.

Finally, to obtain estimated standard uncertainties of refined parameters, blocked full-matrix least-squares refinement was performed, using blocks of 20 residues.

Refinement tests using a 5% cross-validation set showed that restraining the selected hydrogen atoms to riding positions produced essentially identical R and R_{free} values and did not alter the geometrical conclusions presented below (data not shown).

4.6. Figure preparation

Fig. 1a was prepared using the TopDraw sketching tool (Bond, 2003) included in the CCP4 software suite (Agirre et al., 2023). Fig. 1b and c and Figs. 2, 4–6were prepared using PyMOL (The PyMOL Molecular Graphics System, Version 3.0 Schrödinger, LLC).

Abbreviations

CI-2A	chymotrypsin inhibitor 2 A
nat100K	structure of the alcalase–CI-2A complex determined at 100 K
nat277K	structure of the alcalase–CI-2A complex determined at 277 K
mut100K	structure of the alcalase–CI-2A(M59P) complex determined at 100 K
P1–P1'	scissile peptide bond
LBHB	low-barrier hydrogen bond
r.m.s.	root-mean square
e.s.u.	estimated standard uncertainty

CRediT authorship contribution statement

Joanna E. Raczynska: Writing – original draft, Visualization, Investigation, Conceptualization. **Robert Jedrzejczak:** Investigation. **Miroslawa Dauter:** Investigation. **Peter R. Østergaard:** Investigation, Conceptualization. **Keith S. Wilson:** Supervision, Project administration. **Wojciech Rypniewski:** Writing – original draft, Supervision, Project administration, Investigation, Formal analysis, Data curation, Conceptualization.

Declaration of competing interest

The authors declare that they have no known competing financial interests or personal relationships that could have appeared to influence the work reported in this paper.

Appendix A. Supplementary data

Supplementary data to this article can be found online at https://doi.org/10.1016/j.jsb.2026.108377.

Data availability

Research Link Provided
PDB ID: 31VH, 31VI and 31VJ. (Original data) (Protein Data Bank)

References

Agback, P., Agback, T., 2018. Direct evidence of a low barrier hydrogen bond in the catalytic triad of a serine protease. Sci. Rep. 8, 10078. https://doi.org/10.1038/s41598-018-28441-7.

Agirre, J., Atanasova, M., Bagdonas, H., Ballard, C.B., Baslé, A., Beilsten-Edmands, J., Borges, R.J., Brown, D.G., Burgos-Mármol, J.J., Berrisford, J.M., Bond, P.S., Caballero, I., Catapano, L., Chojnowski, G., Cook, A.G., Cowtan, K.D., Croll, T.I., Debreczeni, J.É., Devenish, N.E., Dodson, E.J., Drevon, T.R., Emsley, P., Evans, G., Evans, P.R., Fando, M., Foadi, J., Fuentes-Montero, L., Garman, E.F., Gerstel, M., Gildea, R.J., Hatti, K., Hekkelman, M.L., Heuser, P., Hoh, S.W., Hough, M.A., Jenkins, H.T., Jiménez, E., Joosten, R.P., Keegan, R.M., Keep, N., Krissinel, E.B., Kolenko, P., Kovalevskiy, O., Lamzin, V.S., Lawson, D.M., Lebedev, A.A., Leslie, A.G.W., Lohkamp, B., Long, F., Malý, M., McCoy, A.J., McNicholas, S.J., Medina, A., Millán, C., Murray, J.W., Murshudov, G.N., Nicholls, R.A., Noble, M.E.M., Oeffner, R., Pannu, N.S., Parkhurst, J.M., Pearce, N., Pereira, J., Perrakis, A., Powell, H.R., Read, R.J., Rigden, D.J., Rochira, W., Sammito, M., Sánchez Rodríguez, F., Sheldrick, G.M., Shelley, K.L., Simkovic, F., Simpkin, A.J., Skubak, P., Sobolev, E., Steiner, R.A., Stevenson, K., Tews, I., Thomas, J.M.H., Thorn, A., Valls, J.T., Uski, V., Usón, I., Vagin, A., Velankar, S., Vollmar, M., Walden, H., Waterman, D., Wilson, K.S., Winn, M.D., Winter, G., Wojdyr, M., Yamashita, K., 2023. The CCP4 suite: integrative software for macromolecular crystallography. Acta Cryst D 79, 449–461. https://doi.org/10.1107/S2059798323003595.

Ash, E.L., Sudmeier, J.L., Day, R.M., Vincent, M., Torchilin, E.V., Haddad, K.C., Bradshaw, E.M., Sanford, D.G., Bachovchin, W.W., 2000. Unusual 1H NMR chemical shifts support (His) C(epsilon) 1...O==C H-bond: proposal for reaction-driven ring flip mechanism in serine protease catalysis. Proc. Natl. Acad. Sci. U. S. A. 97, 10371–10376. https://doi.org/10.1073/pnas.97.19.10371.

Bond, C.S., 2003. TopDraw: a sketchpad for protein structure topology cartoons. Bioinformatics 19, 311–312. https://doi.org/10.1093/bioinformatics/19.2.311.

Cleland, W.W., Frey, P.A., Gerlt, J.A., 1998. The low barrier hydrogen bond in enzymatic catalysis. J. Biol. Chem. 273, 25529–25532. https://doi.org/10.1074/jbc.273.40.25529.

Derewenda, Z.S., Derewenda, U., Kobos, P.M., 1994. (His)C epsilon-H...O=C < hydrogen bond in the active sites of serine hydrolases. J. Mol. Biol. 241, 83–93. https://doi.org/10.1006/jmbi.1994.1475.

Di Cera, E., 2009. Serine proteases. IUBMB Life 61, 510–515. https://doi.org/10.1002/iub.186.

Du, S., Kretsch, R.C., Parres-Gold, J., Pieri, E., Cruzeiro, V.W.D., Zhu, M., Pinney, M.M., Yabukarski, F., Schwans, J.P., Martínez, T.J., Herschlag, D., 2025. Conformational ensembles reveal the origins of serine protease catalysis. Science 387, eado5068. https://doi.org/10.1126/science.ado5068.

Emsley, P., Lohkamp, B., Scott, W.G., Cowtan, K., 2010. Features and development of coot. Acta crystallographica. Section D, Biological crystallography 66, 486–501. https://doi.org/10.1107/S0907444910007493.

Frey, P.A., 2004. Strong hydrogen bonding in chymotrypsin and other serine proteases. J. Phys. Org. Chem. 17, 511–520. https://doi.org/10.1002/poc.769.

Frey, P.A., Whitt, S.A., Tobin, J.B., 1994. A low-barrier hydrogen bond in the catalytic triad of serine proteases. Science 264, 1927–1930. https://doi.org/10.1126/science.7661899.

Fuhrmann, C.N., Daugherty, M.D., Agard, D.A., 2006. Subangstrom crystallography reveals that short ionic hydrogen bonds, and not a His-Asp low-barrier hydrogen Bond, stabilize the transition state in serine protease catalysis. J. Am. Chem. Soc. 128, 9086–9102. https://doi.org/10.1021/ja057721o.

Hedstrom, L., 2002. Serine protease mechanism and specificity. Chem. Rev. 102, 4501–4524. https://doi.org/10.1021/cr000033x.

Ishida, T., 2006. Low-barrier hydrogen bond hypothesis in the catalytic triad residue of serine proteases: correlation between structural rearrangement and chemical shifts in the acylation process. Biochemistry 45, 5413–5420. https://doi.org/10.1021/bi051515b.

Ishida, T., Kato, S., 2003. Theoretical perspectives on the reaction mechanism of serine proteases: the reaction free energy profiles of the acylation process. J. Am. Chem. Soc. 125, 12035–12048. https://doi.org/10.1021/ja021369m.

Juers, D.H., Matthews, B.W., 2001. Reversible lattice repacking illustrates the temperature dependence of macromolecular interactions. J. Mol. Biol. 311, 851–862. https://doi.org/10.1006/jmbi.2001.4891.

Juers, D.H., Matthews, B.W., 2004. Cryo-cooling in macromolecular crystallography: advantages, disadvantages and optimization. Q. Rev. Biophys. https://doi.org/10.1017/s0033583504004007.

Kemp, M.T., Lewandowski, E.M., Chen, Y., 2021. Low barrier hydrogen bonds in protein structure and function. Biochim. Biophys. Acta, Proteins Proteomics 1869, 140557. https://doi.org/10.1016/j.bbapap.2020.140557.

Kuhn, P., Knapp, M., Soltis, S.M., Ganshaw, G., Thoene, M., Bott, R., 1998. The 0.78 Å structure of a serine protease: *Bacillus lentus* subtilisin. Biochemistry 37, 13446–13452. https://doi.org/10.1021/bi9813983.

Langer, G.G., Cohen, S.X., Lamzin, V.S., Perrakis, A., 2008. Automated macromolecular model building for X-ray crystallography using ARP/wARP version 7. Nat. Protoc. 3, 1171–1179. https://doi.org/10.1038/nprot.2008.91.

McPhalen, C.A., James, M.N., 1987. Crystal and molecular structure of the serine proteinase inhibitor CI-2 from barley seeds. Biochemistry 26, 261–269. https://doi.org/10.1021/bi00375a036.

Murshudov, G.N., Skubák, P., Lebedev, A.A., Pannu, N.S., Steiner, R.A., Nicholls, R.A., Winn, M.D., Long, F., Vagin, A.A., 2011. REFMAC5 for the refinement of macromolecular crystal structures. Acta Crystallogr. D Biol. Crystallogr. 67, 355. https://doi.org/10.1107/S0907444911001314.

Navaza, J., 2001. Implementation of molecular replacement in AMoRe. Acta Cryst D 57, 1367–1372. https://doi.org/10.1107/S0907444901012422.

Otwinowski, Z., Minor, W., 1997. Processing of X-ray diffraction data collected in oscillation mode. Methods in Enzymology. Elsevier, pp. 307–326. https://doi.org/10.1016/S0076-6879(97)76066-X.

Radisky, E.S., Koshland, D.E., 2002. A clogged gutter mechanism for protease inhibitors. Proc. Natl. Acad. Sci. 99, 10316–10321. https://doi.org/10.1073/pnas.112332899.

Radisky, E.S., Kwan, G., Karen Lu, C.-J., Koshland, D.E., 2004. Binding, proteolytic, and crystallographic analyses of mutations at the protease-inhibitor interface of the subtilisin BPN'/chymotrypsin inhibitor 2 complex. Biochemistry 43, 13648–13656. https://doi.org/10.1021/bi048797k.

Radisky, E.S., Lu, C.-J.K., Kwan, G., Koshland, D.E., 2005. Role of the intramolecular hydrogen Bond network in the inhibitory power of chymotrypsin inhibitor 2. Biochemistry 44, 6823–6830. https://doi.org/10.1021/bi047301w.

Schiøtt, B., Iversen, B.B., Madsen, G.K., Larsen, F.K., Bruice, T.C., 1998. On the electronic nature of low-barrier hydrogen bonds in enzymatic reactions. Proc. Natl. Acad. Sci. U. S. A. 95, 12799–12802. https://doi.org/10.1073/pnas.95.22.12799.

Schutz, C.N., Warshel, A., 2004. The low barrier hydrogen bond (LBHB) proposal revisited: the case of the Asp. His pair in serine proteases. Proteins 55, 711–723. https://doi.org/10.1002/prot.20096.

Sheldrick, G.M., 2015. Crystal structure refinement with SHELXL. Acta Cryst C 71, 3–8. https://doi.org/10.1107/S2053229614024218.

Smith, E.L., DeLange, R.J., Evans, W.H., Landon, M., Markland, F.S., Subtilisin Carlsberg., V., 1968. The complete sequence; comparison with subtilisin BPN'; evolutionary relationships. J. Biol. Chem. 243, 2184–2191. https://doi.org/10.1016/S0021-9258(18)93461-7.

Stachowski, T.R., Fischer, M., 2026. Unfreezing structural biology for drug discovery. Nat. Chem. Biol. 22, 169–179. https://doi.org/10.1038/s41589-025-02047-3.

Topf, M., Richards, W.G., 2004. Theoretical studies on the deacylation step of serine protease catalysis in the gas phase, in solution, and in elastase. J. Am. Chem. Soc. 126, 14631–14641. https://doi.org/10.1021/ja047010a.

Topf, M., Várnai, P., Richards, W.G., 2002. Ab initio QM/MM dynamics simulation of the tetrahedral intermediate of serine proteases: insights into the active site hydrogen-bonding network. J. Am. Chem. Soc. 124, 14780–14788. https://doi.org/10.1021/ja026219q.

Wei, W., Chen, Y., Xie, D., Zhou, Y., 2019. Molecular insight into chymotrypsin inhibitor 2 resisting proteolytic degradation. Phys. Chem. Chem. Phys. 21, 5049–5058. https://doi.org/10.1039/c8cp07784c.

Winn, M.D., Ballard, C.C., Cowtan, K.D., Dodson, E.J., Emsley, P., Evans, P.R., Keegan, R.M., Krissinel, E.B., Leslie, A.G.W., McCoy, A., McNicholas, S.J., Murshudov, G.N., Pannu, N.S., Potterton, E.A., Powell, H.R., Read, R.J., Vagin, A., Wilson, K.S., 2011. Overview of the CCP4 suite and current developments. Acta crystallographica. Section D, Biological crystallography 67, 235–242. https://doi.org/10.1107/S0907444910045749.